AD-A131 628 DESIGN AND OPERATION OF A COLLECTIVE MILLIMETER-WAVE FREE-ELECTRON LASER(U) NAVAL RESEARCH LAB WASHINGTON DC R H JACKSON ET AL. 27 JUL 83 NRL-MR-5076 1/1

UNCLASSIFIED F/G 20/6 NL

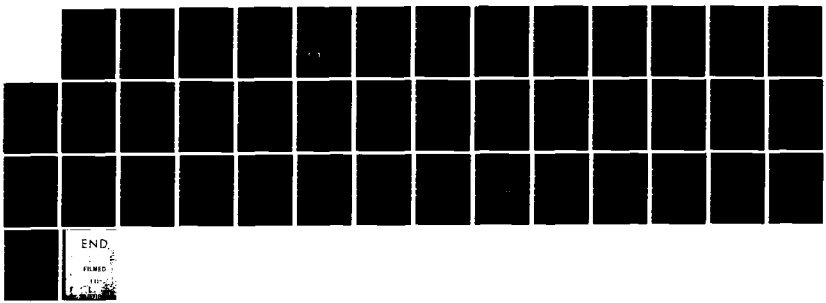

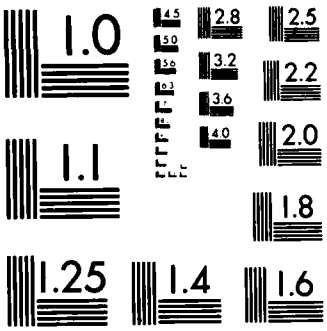

MICROCOPY RESOLUTION TEST CHART
NATIONAL BUREAU OF STANDARDS-1963-A

(2)

NRL Memorandum Report 5076

AD A131628

Design and Operation of a Collective Millimeter-Wave Free-Electron Laser

R. H. JACKSON,* S. H. GOLD, R. K. PARKER,** H. P. FREUND,†
P. C. EFTHIMION,‡ V. L. GRANATSTEIN, M. HERNDON,
A. K. KINKEAD, J. E. KOSAKOWSKI,§ AND T. J. T. KWAN††

High Power Electromagnetic Radiation Branch
Plasma Physics Division

**Mission Research Corporation*
Alexandria, VA 22312

***Microwave and Millimeter Wave Tube Techniques Branch*
Electronics Technology Division

†Science Applications, Inc.
McLean, VA 22102

‡JAYCOR, Inc.
Alexandria, VA 22304

§Sachs-Freeman Assoc., Inc.
Bowie, MD 20715

††Los Alamos National Laboratory
Los Alamos, NM 87545

July 27, 1983

This research was supported by the Naval Air Systems Command and the Air Force Office of Scientific Research.

DTIC
ELECTE
AUG 22 1983
S B

NAVAL RESEARCH LABORATORY
Washington, D.C.

Approved for public release; distribution unlimited.

DTIC FILE COPY

83 08 19 097

SECURITY CLASSIFICATION OF THIS PAGE (When Data Entered)

REPORT DOCUMENTATION PAGE		READ INSTRUCTIONS BEFORE COMPLETING FORM
1. REPORT NUMBER NRL Memorandum Report 5076	2. GOVT ACCESSION NO.	3. RECIPIENT'S CATALOG NUMBER
4. TITLE (and Subtitle) DESIGN AND OPERATION OF A COLLECTIVE MILLIMETER-WAVE FREE-ELECTRON LASER		5. TYPE OF REPORT & PERIOD COVERED Interim report on a continuing NRL problem. 6. PERFORMING ORG. REPORT NUMBER
7. AUTHOR(s) R.H. Jackson,* S.H. Gold, R.K. Parker, H.P. Freund†, P.C. Efthimion,‡ V.L. Granatstein, M. Herndon,¶ A.K. Kinkead, J.E. Kosakowski,§ and T.J.T. Kwan††		8. CONTRACT OR GRANT NUMBER(s)
9. PERFORMING ORGANIZATION NAME AND ADDRESS Naval Research Laboratory Washington, D.C. 20375		10. PROGRAM ELEMENT, PROJECT, TASK AREA & WORK UNIT NUMBERS 62768N; SF68-342-602; 68-1839-A-3
11. CONTROLLING OFFICE NAME AND ADDRESS		12. REPORT DATE July 27, 1983 13. NUMBER OF PAGES 40
14. MONITORING AGENCY NAME & ADDRESS(if different from Controlling Office)		15. SECURITY CLASS. (of this report) UNCLASSIFIED 15a. DECLASSIFICATION/DOWNGRADING SCHEDULE

16. DISTRIBUTION STATEMENT (of this Report)

Approved for public release; distribution unlimited.

17. DISTRIBUTION STATEMENT (of the abstract entered in Block 20, if different from Report)

18. SUPPLEMENTARY NOTES

*Present address: Mission Research Corporation, Alexandria, VA 22312
†Present address: Science Applications, Inc., McLean, VA 22102
‡Present address: JAYCOR, Inc., Alexandria, VA 22304
¶Deceased

(Continues)

19. KEY WORDS (Continue on reverse side if necessary and identify by block number)

Microwave generation
Millimeter-wave sources
Power amplifiers
Ubitrons
Free electron laser

20. ABSTRACT (Continue on reverse side if necessary and identify by block number)

A new free-electron laser experiment has been designed at NRL to operate at millimeter wavelengths using a collective beam-wave interaction. Critical features of the experiment include an apertured diode which provides a low emittance electron beam, a wiggler magnet with adiabatic entrance and exit, and an operational domain centered around the wiggler-guide field gyroresonance. With the experiment configured as a superradiant amplifier, the effects of the gyroresonance on beam dynamics and the beam-wave interaction have been studied. Measurements indicate a peak power production of 35 MW at 4 mm

(Continues)

DD FORM 1 JAN 73 1473 EDITION OF 1 NOV 65 IS OBSOLETE
S/N 0102-014-6601

SECURITY CLASSIFICATION OF THIS PAGE (When Data Entered)

18. SUPPLEMENTARY NOTES (Continued)

§Present address: Sachs-Freeman Assoc., Inc., Bowie, MD 20715
††Present address: Los Alamos National Laboratory, Los Alamos, NM 87545

This research was supported by the Naval Air Systems Command and the Air Force Office of Scientific Research.

20. ABSTRACT (Continued)

with an electronic efficiency of 2.5%. Aspects of the experimental design are discussed, and the results of a parametric study of the power dependence on the fields are presented. Detailed calculations (both analytic and computational) have been performed to analyze the linear and nonlinear effects in the experiment. The results of these calculations are shown to be in good agreement with laboratory measurements.

CONTENTS

I. INTRODUCTION 1

II. EXPERIMENTAL APPARATUS 3

III. THEORY 15

IV. EXPERIMENTAL RESULTS 29

V. SUMMARY 34

ACKNOWLEDGMENTS 34

REFERENCES 35

DTIC
ELECTE
AUG 22 1983
S D
B

Accession For
NTIS GRA&I ☑
DTIC TAB ☐
Unannounced ☐
Justification

By
Distribution/
Availability Codes
Dist | Avail and/or Special
A

DESIGN AND OPERATION OF A COLLECTIVE MILLIMETER-WAVE FREE-ELECTRON LASER

R. H. Jackson*, S. H. Gold, R. K. Parker, H. P. Freund**,
P. C. Efthimion†, V. L. Granatstein, M. Herndon††, A. K. Kinkead,
and J. E. Kosakowski§
Naval Research Laboratory
Washington, DC 20375
(202) 767-6655
and

T. J. T. Kwan
Los Alamos National Laboratory
Los Alamos, NM 87545
(505) 667-3447

I. Introduction

The free electron laser has become the subject of intensive research because of its potential as an efficient, high-power source of continuously tunable coherent radiation. Essentially, the free electron laser is a linear fast-wave device in which a signal wave is amplified at the expense of the axial kinetic energy of a codirectional relativistic electron beam through interaction with the periodic transverse field of a "wiggler" or pump magnet. The output wavelength is related to the wiggler period by the approximate relationship $\lambda_o \approx \lambda_w/2\gamma^2$, where λ_o and λ_w are respectively the output wavelength and wiggler period and γ is the relativistic mass factor. This frequency upshift provides an obvious advantage for high-frequency power production.

*North Carolina State University, Raleigh, North Carolina 27650.
Present address: Mission Research Corporation, Alexandria, VA 22312.
**Permanent address: Science Applications, Inc., McLean, VA 22102.
†Also at JAYCOR, Inc., Alexandria, VA 22304.
††Deceased.
§Permanent address: Sachs-Freeman Assoc. Inc., Bowie, MD 20715.
Manuscript approved March 2, 1983.

Within the range of available electron beam and wiggler technologies, free-electron lasers can be designed such that the beam-wave interaction can be dominated by either single particle or collective effects. If the Debye length of the electron beam is less than the wavelength, collective effects dominate and the resultant three-wave parametric interaction is described as stimulated Raman scattering. This relationship leads to a requirement for a high electron density and a small spread in the axial velocity distribution of the electron beam. More specifically, the axial velocity spread must be much less than $\lambda_w \omega_p (\gamma - 1)/4\pi \gamma \gamma_z$, where ω_p is the invariant plasma frequency, $\gamma = (1 - \beta^2)^{-1/2}$, $\beta = v/c$, $\gamma_z \equiv (1 - \beta_z)^{-1/2}$, $\beta_z = v_z/c$, c is the speed of light. In practical terms, this constraint means that considerable care must be taken to control the beam emittance if intense beam experiments conducted at millimeter and submillimeter wavelengths are to exhibit wave-wave scattering.

When collective effects are dominant, positive gain is achieved when the pump-shifted, negative-energy, space-charge wave is synchronous with an appropriate waveguide mode. The primary advantage of wave-wave scattering is that it offers significantly higher gain and intrinsic electronic efficiency than can be obtained with wave-particle (Compton) scattering. The higher gain of the collective interaction is sufficient to make amplifier operation practical. Calculations, based on an idealized model[1], indicate that electronic efficiencies in excess of 10% and power exponentiation lengths of several centimeters are achievable at millimeter wavelengths.

Critical performance features predicted for the collective interaction have not been demonstrated in previous experiments. Although exceptionally high peak powers have been reported, the corresponding gains and efficiencies have been comparatively low. In an early stimulated scattering experiment conducted at NRL[2], a superradiant output of 1 MW at 0.4 mm was generated with an approximate efficiency of 10^{-3}% using an electromagnetic pump wave. A subsequent oscillator experiment[3] with a magnetostatic pump produced a comparable peak power at the same frequency with an efficiency of 3×10^{-3}%. In other experiments, peak powers of 8 MW at 1.5 mm and 20 MW at 11 mm with corresponding efficiencies of 0.2% and 0.3% have been reported.[4,5]

Recent computational analysis of the electron flow in the cold-cathode diodes typically used in these experiments has indicated that poor beam quality likely had a strong influence on observed performance[6]. Recognition of the constraints on beam quality led to the assembly of a new experimental configuration designed to study the Raman interaction at millimeter wavelengths[7]. With this apparatus, the combined effects of the axial guide and helical wiggler magnetic fields on the electron dynamics and the beam-wave interaction have been studied in initial experiments. These effects are of interest because a significant gain enhancement can be obtained near the gyroresonance which occurs when the electron transit time through a wiggler period corresponds to one cyclotron period.

II. Experimental Apparatus

A. Experimental Configuration

For these studies, the VEBA pulse-line accelerator was modified[8] and interaction parameters were selected to ensure a collective interaction. Computational analysis produced an injection diode design[9] which provided significantly improved beam quality. As shown in Fig. 1, the diode was formed by locating a cylindrical graphite cathode with hemispherical tip a distance of 1 cm from a shaped graphite anode. A 6-mm-diameter aperture in the anode plate was used to collimate the injected beam. Electrode contours were derived computationally to provide radial force balance for near-axis electron trajectories. With this design, the axial velocity spread of the beam injected through the aperture was reduced to less than 0.1%, which corresponds to a normalized beam emittance of 30π mrad•cm.

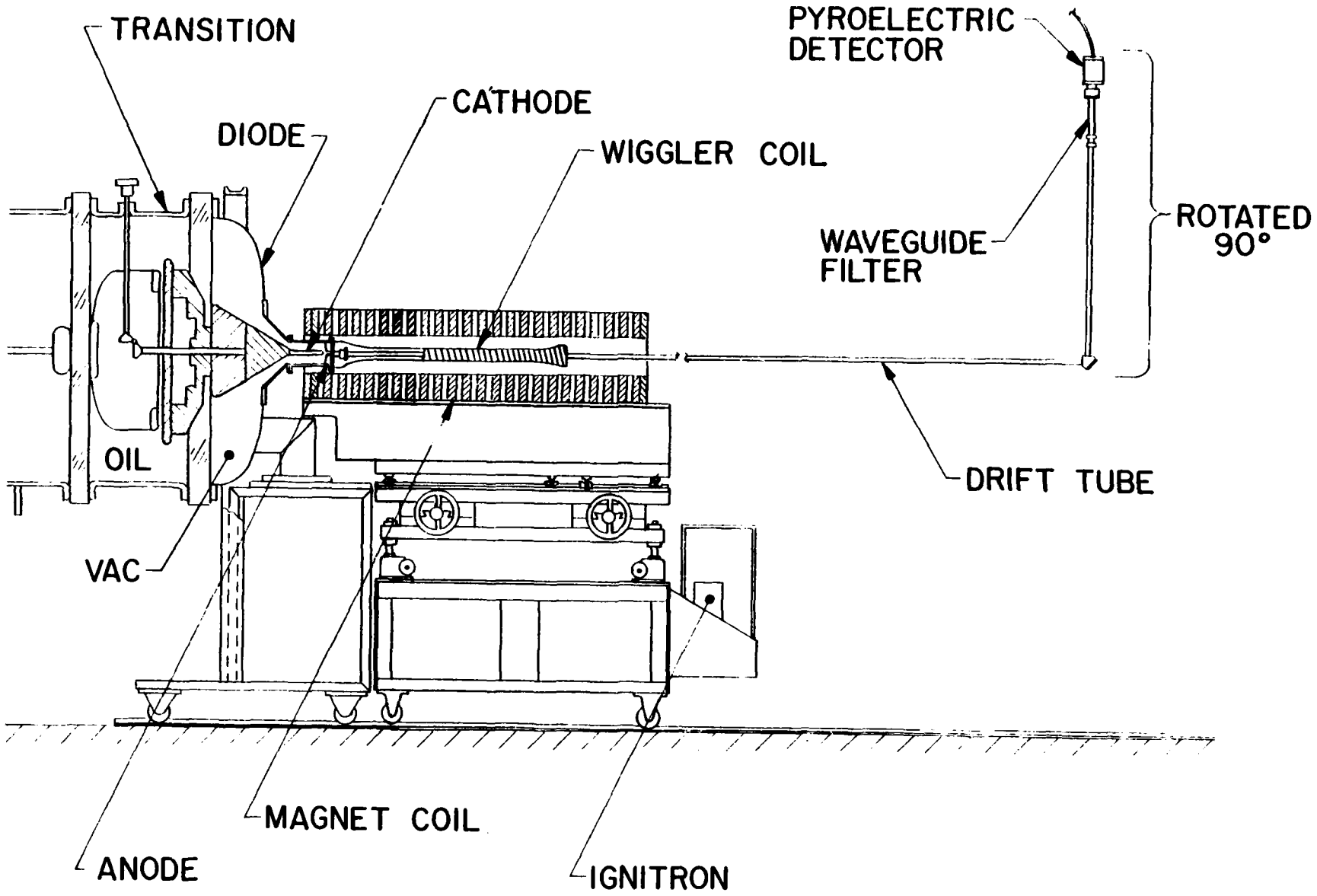

Fig. 1 Experimental setup for superradiant millimeter-wave Raman free-electron laser.

The pump wave was a right-hand-circularly-polarized magnetostatic field produced by a 63-cm long bifilar helix of 3-cm periodicity. The bifilar helix consisted of two coils of copper magnet wire with four layers per coil wound on a grooved nylon form. To prevent perturbation of the beam, a gradual transition into the wiggler field was necessary. A 21-cm transition region was provided by flaring the radius of the helical windings along a circular arc while keeping the period of the windings constant. The windings were joined at the end of the flare by wrapping alternate layers in opposite directions around the nylon form. This counter-winding reduced the magnetic field perturbation caused by the termination of the windings. The measured and calculated[10] fields in the taper are shown in Fig. 2. With the exception of field values near gyroresonance, the adiabaticity condition was well satisfied by the transition field as discussed in the section on theory. In addition a 15-cm adiabatic exit from the wiggler was provided to reduce possible RF noise production resulting from unnecessary perturbation of the beam.

The initial experiments were conducted with the device configured as a superradiant, or noise, amplifier. With 1.35 MV applied to the diode, a 1.5-kA electron beam of 60-nsec duration was extracted through the anode aperture and propagated through a tapered-wall transition into a cylindrical stainless steel waveguide of 1.1-cm inner diameter. The axial magnetic field was held constant from behind the cathode to beyond the interaction space and was variable up to 20 kG. The wiggler field was variable from 0.1 to 4 kG. With this selection of parameters, the beam axial velocity spread had to be much less than 0.5% for collective effects to dominate the interaction.

To provide temporal isolation from reflected signals, the radiation diagnostics were separated from the interaction space by a 5-m length of waveguide. The principal radiation diagnostic was a Laser Precision KT 1540S pyroelectric detector which provided a time dependent measure of radiated power. Absolute integrated power measurements were made using a pyramidal millimeter-wave calorimeter[11] constructed at the laboratory. Spectral information was obtained by sequentially placing a series of high-pass filters in front of the detector. The high-pass filters were cut-off waveguides of two mechanical designs, both fabricated

from aluminum cylinders. The filter designs used either a single axially located hole with tapered entrance and exit or symmetrical arrays of constant diameter holes.

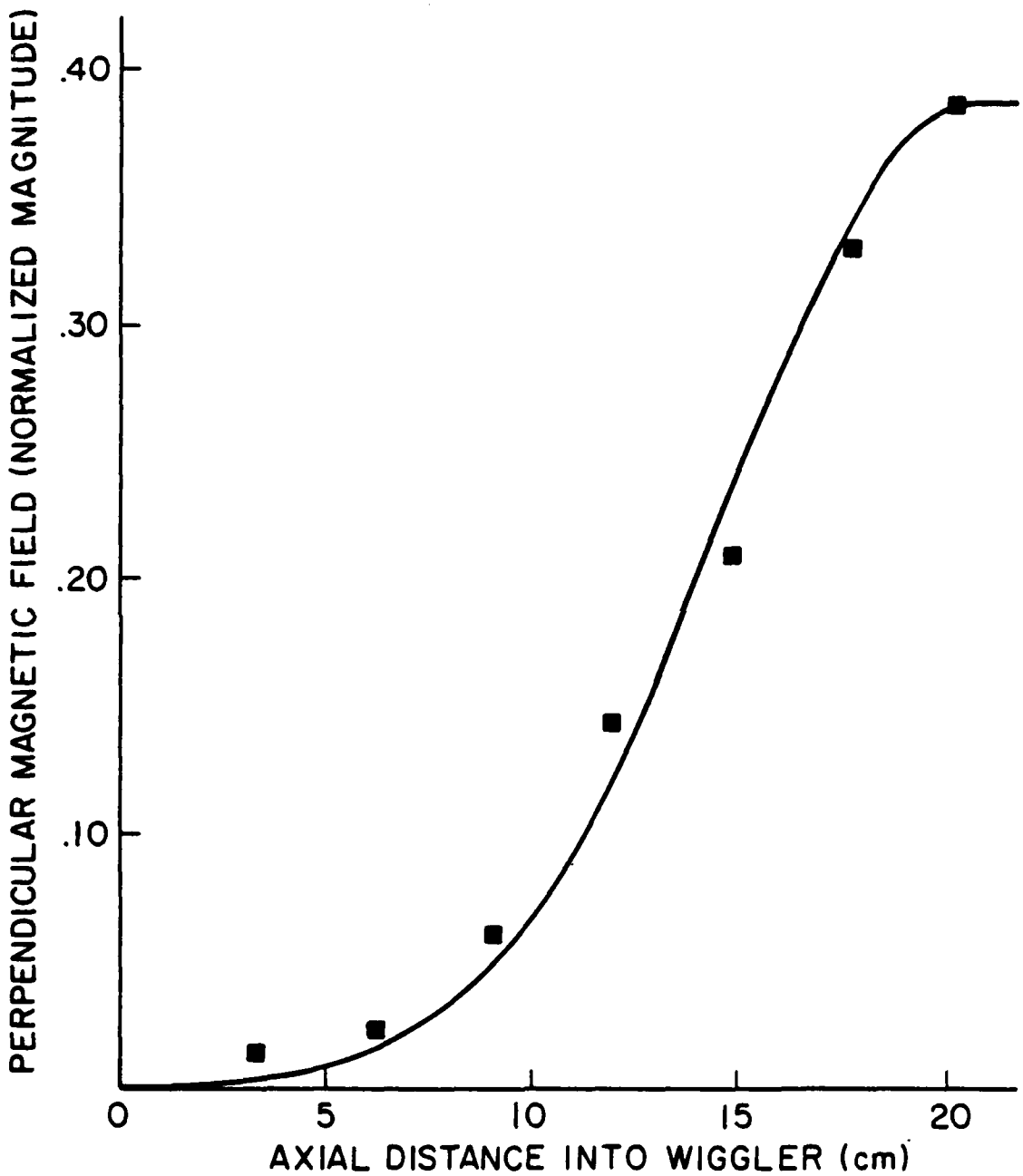

Fig. 2 The on-axis wiggler field profile in the 21-cm adiabatic entrance of the bifilar helix. The solid curve is based on the equations in Ref. 9, and the squares are the normalized measurements.

For these experiments, the beam-wave interaction parameters were chosen such that the pump-shifted negative-energy space-charge wave would couple with the fundamental TE_{11} mode of the cylindrical waveguide. An overlay of the uncoupled beam and waveguide dispersion curves shows that two intersections with the forward wave are possible. Primary interest is centered on the upper intersection, which produces a large relativistic upshift. In the limit $\beta_\perp = 0$ $(\beta_\perp = v_\perp/c)$, this intersection occurs at about 180 GHz, while the lower intersection is at about 20 GHz. The effect of increasing the wiggler field is to increase $\beta_\perp$ while simultaneously decreasing the axial velocity β_z. This shifts the upp intersection to lower frequencies (and the lower intersection upwards until coupling is lost at ≈ 60 GHz for $\beta_\perp \approx .34$. To block the transmission of any low frequency power not associated with the upper intersection, a 5-mm (60 GHz) high-pass filter was inserted near the detector.

B. Diode Design

Theory places severe constraints on the quality of an electron beam for collective processes to dominate the beam-wave interaction. Computational analysis of the foil-less diodes used in previous experiments has shown that the beams taken as a whole did not satisfy the theoretical quality requirement, although in some cases layers within a beam were cold enough to permit marginal collective interaction[6]. Furthermore, the analysis indicated that there are inherent problems in obtaining high quality beams in foil-less diode geometries. Two alternative designs were considered, injection through an anode foil and a collector anode with a beam extraction aperture. The use of an anode foil was considered to be unattractive because of consequent beam scattering in the foil, the necessity for replacement of foils after every shot, and resultant beam pinching in the diode. Analytic and computational analysis of the apertured diode indicated that this approach could provide the required beam quality.

The apertured diode was designed using a modified version[11] of the SLAC Electron Optics Code[12]. The objective was to produce paraxial electron flow in the diode near the axis by shaping the electrode surfaces to provide a radial electric field to balance the pinching effects of the beam self B_θ field. Since the cathodic electric fields were too high to control the emitting surface, it was necessary to collect the excess current ($\approx$ 90%) and allow only the cold, near-axis portion of the beam to propagate into the interaction region. The final diode design, along with the computed electron trajectories, is shown in Fig. 3. In this design the cathode was a graphite cylinder with a hemispherical tip. To keep the emitting surface small and the diode impedance high, the cathode tip had a radius of curvature of 2.5 cm on the face and 0.5 cm on the edge. The anode was a graphite disk with a 10° conical depression and a 6-mm diameter aperture on axis. The aperture was extended 15 cm into the interaction region with a gradual taper to the 11-mm diameter of the cylindrical waveguide. Because the 1-cm diode gap was sensitive to voltage prepulse[13], a dielectric surface-flashover switch[11] was installed in the cathode shank. The switch eliminated prepulse problems and, in addition, sharpened the voltage rise time. The reduced rise time enhanced the formation of a homogeneous, uniformly expanding cathode plasma, and thereby acted to preserve the basic diode geometry. The importance of eliminating prepulse problems was illustrated by two experimental observations. First, when a prepulse current occurred, the beam noise (no wiggler) in W-band jumped by more than an order of magnitude. Secondly, with the wiggler field, power output was greatly reduced when even small prepulse currents occurred. These observations indicate a reduced beam quality when the cathode plasma formation is not rapid and uniform.

The calculated trajectories shown in Fig. 3 represent the electron flow expected for a guide field of 10 kG and an applied voltage of 1.5 MV. The "grid" in the figure is a computational device used to give a physically meaningful boundary condition to the electron emission from the cathode shank while avoiding the problems of resolving the crossed-field flow. The net effect of the applied and self-generated fields is to produce an electron flow near the axis which exhibits little

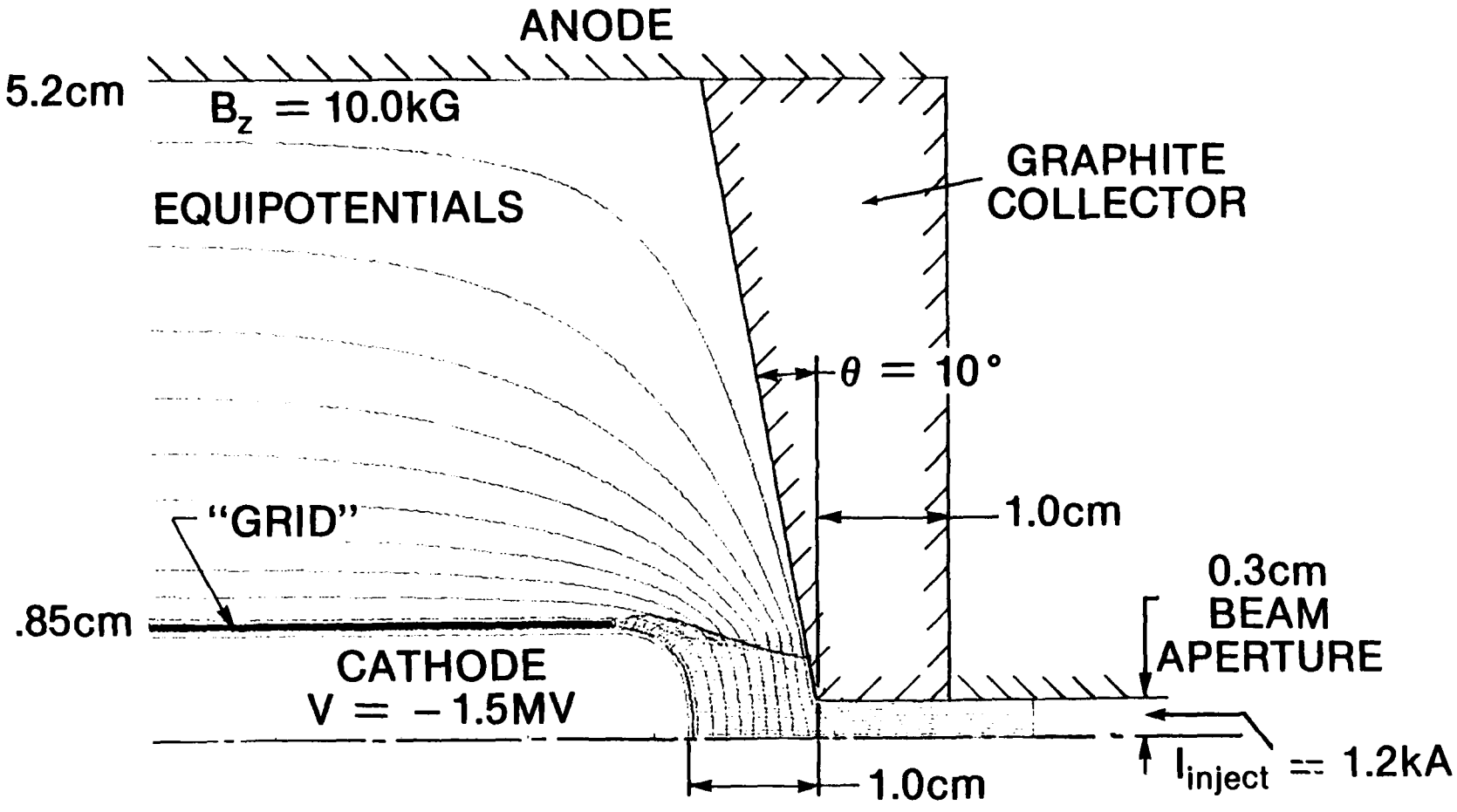

Fig. 3 The VEBA apertured diode with the calculated electron trajectories (only half of the trajectories are shown). Note the paraxial flow close to the axis between the cathode and anode, and the defocusing effect of the aperture.

radial motion until the aperture is reached. The radial electrostatic fields created by the aperture then act to defocus the beam and produce a small, coherent radial oscillation in the extracted beam. Results from these calculations indicated that beams with less than 0.1% axial velocity spread could be produced with the apertured diode configuration.

Where possible, code results were compared with laboratory measurements to validate the calculations. In comparing the calculated and experimental values, it should be noted that the code dealt with the "cold" geometry, whereas the effective cathode in the experiment was an expanding plasma. The initial comparisons were made with respect to two parameters which describe the macroscopic properties of the electron flow in the diode. These parameters are the diode perveance[14] and the current transmitted through the aperture. The perveance is calculated from the total diode current and voltage and is shown in Fig. 4 as a function of the axial guide field. The decrease in perveance with increased guide field indicates a change in the effective diode geometry. The observed reduction results from the restricted radial expansion of the electron trajectories and the cathode plasma at the higher fields. At low guide fields where the entire diode gap decreases, the difference between the computed and observed perveance can be used to estimate the plasma expansion velocity. For the values at 2 kG, this gives an expansion velocity of 2-3 cm/μsec which is in good agreement with previous measurements[15].

As the magnetic field is increased, the cathode plasma does not continue to expand at the same rate in all directions. However, the field strength should have no effect on the axial expansion at the cathode face. The effect of cathode expansion on extracted current is apparent in Fig. 5. At the higher magnetic fields, the plasma expansion velocity derived from these values is also consistent with a 2-3 cm/μsec expansion velocity. Plasma expansion at the lower field levels (< 8 kG) does not show as large an effect because the current is limited by aperture defocusing and not by the available current.

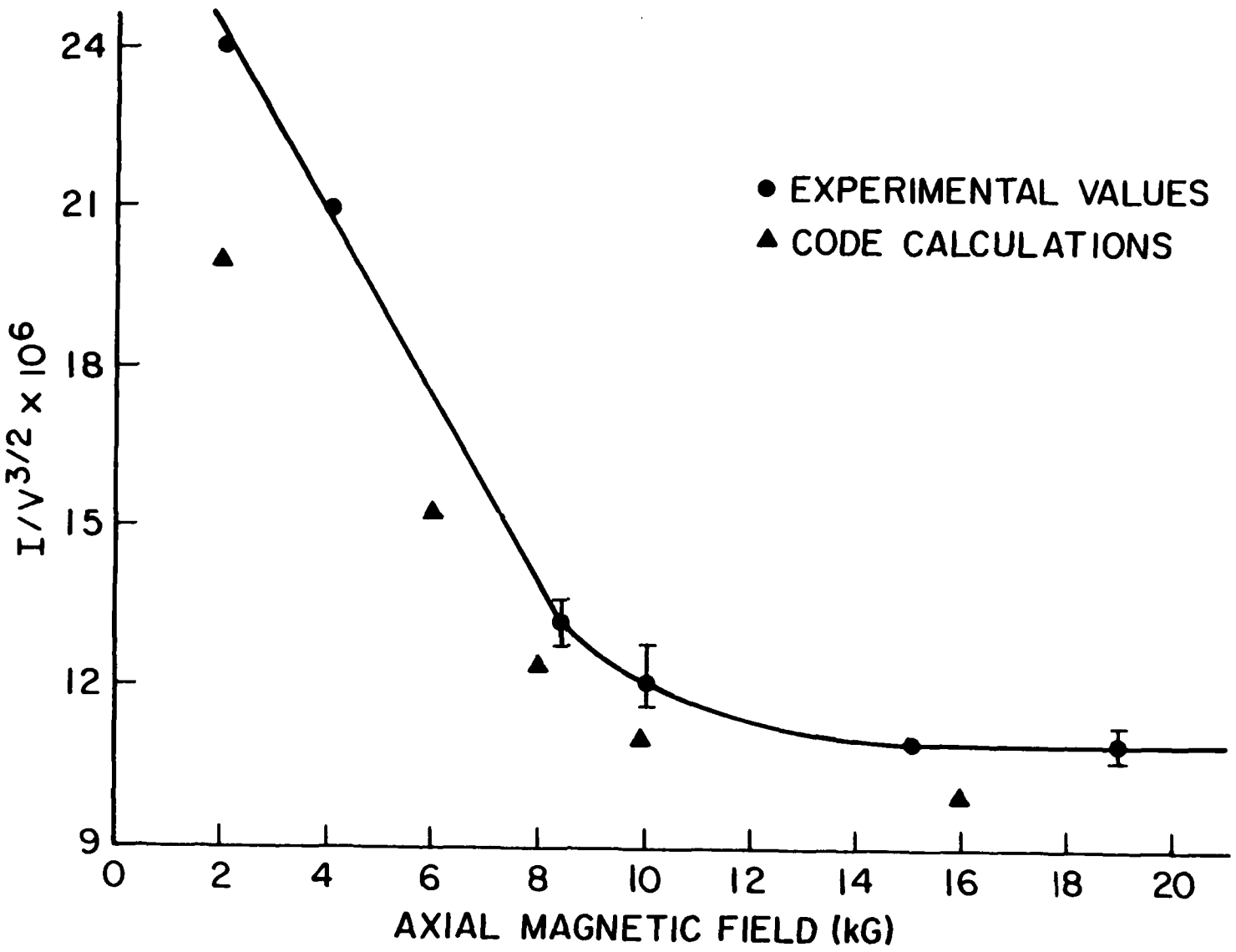

Fig. 4 Perveance of the apertured diode as a function of axial guide field.

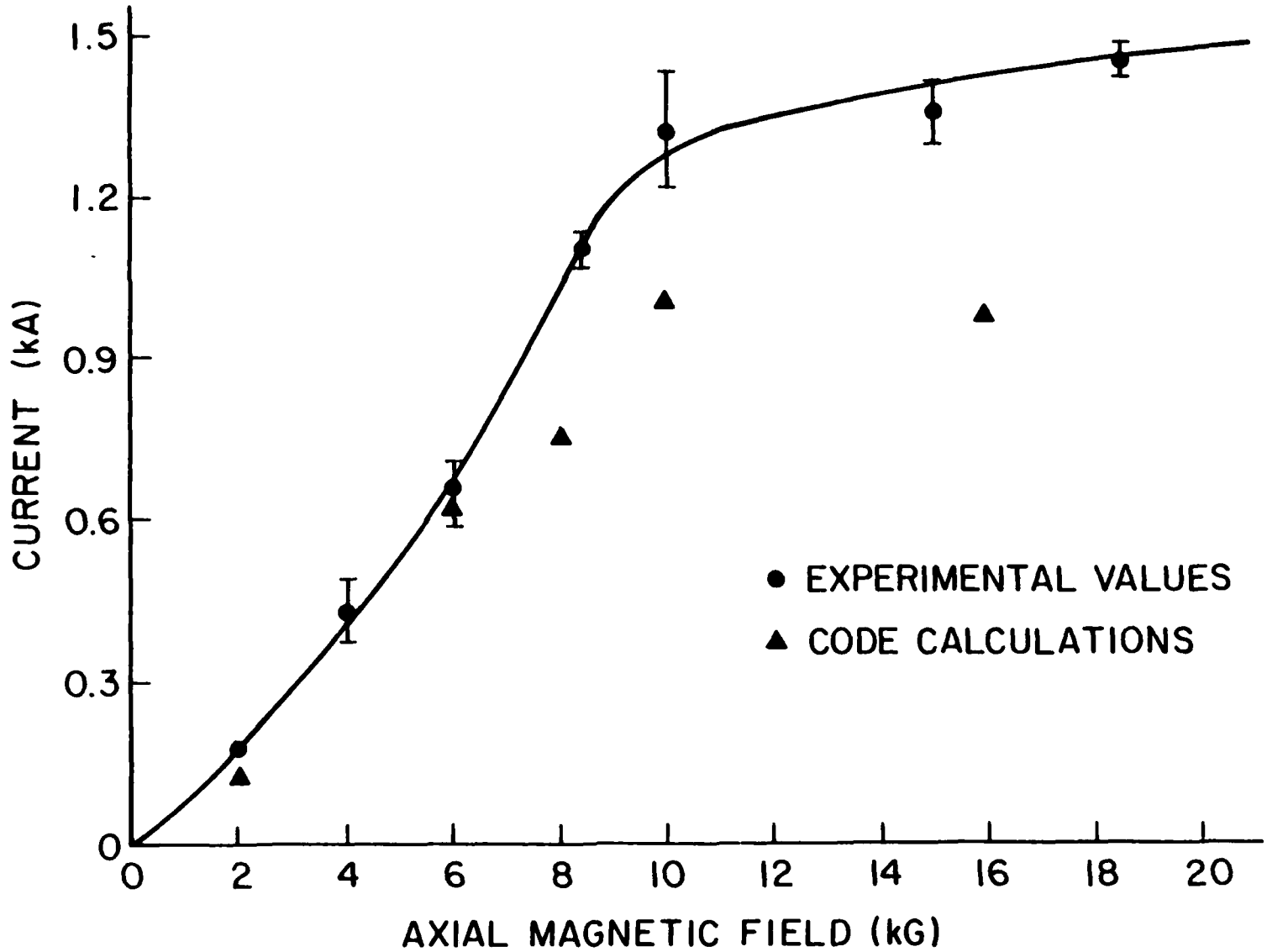

Fig. 5 The current transmitted through the diode aperture as a function of axial guide field.

C. Beam Quality Measurements

When corrected for plasma expansion, the predicted values of diode perveance and transmitted current are in excellent agreement with experimental measurements. Although the comparison of macroscopic features provides a tentative verification of the computed results, the more critical issue is the velocity distribution within the transmitted beam. In general, experimental measurement of the velocity distribution within an intense, relativistic electron beam is extremely difficult. However, using the special properties of the apertured diode, a simple method was devised to experimentally verify the code results. For these measurements, the 6-mm-diameter anode aperture was extended by 15 cm with a uniform diameter drift tube which terminated in a Faraday cup. The perpendicular velocity of electrons at the beam edge was then calculated by comparing the transmitted current at a given value of axial magnetic field (Fig. 5) with that estimated for an infinite field. The axial velocity spread was then derived from the beam-edge transverse velocity. This analysis requires that the cathode tip emission density and the electron guiding center radius be independent of the axial field, and that the beam be monoenergetic. Analysis of results computed at several values of the guide field indicate that these conditions were well satisfied. In addition, a uniform beam density is assumed, although this method could still be used if the density profile were known. Code results and experimental damage patterns have shown that the assumption of a uniform beam was a good approximation.

The relationship between transmitted current and axial velocity spread was derived as follows. In the limit of an infinite field, the electron Larmor radius is zero. As the field is reduced, the electron guiding center remains unchanged, but the Larmor radius becomes finite. Only those electrons for which the sum of the Larmor and guiding center radii is less than the aperture radius can be propagated. The current ratio is therefore given by

$$I(B_o)/I(\infty) = (r_w - r_L)^2/r^2_w \qquad (1)$$

where r_w and r_L are respectively the drift tube wall and Larmor radii, B_o is the axial guide field, and $I(\infty)$ is the transmitted current in the limit of infinite magnetic field. When solved for the perpendicular velocity, this expression becomes

$$\beta_\perp = \{1 - [I(B_o)/I(\infty)]^{1/2}\} e\, B_o r_w / mc^2 \gamma \qquad (2)$$

Numerical analysis of electron trajectories in the diode and drift tube verifies this prediction of the electron perpendicular velocity at the beam periphery. The axial and transverse velocity spreads are related as follows:

$$\Delta\beta_z/\beta_z \approx (\Delta\beta_\perp)^2/2\beta^2 \approx [\beta_\perp(r_w)]^2/4\beta^2 \qquad (3)$$

With this relationship, the transverse velocity at the beam periphery can be used to estimate the axial velocity spread. As seen in (2), a measure of $I(\infty)$ is required to complete the estimate. As a lower bound, the transmitted current at 20 kG was measured to be 1.5 kA. The Child-Langmuir current, when corrected for cathode plasma expansion, serves as a reasonable upper bound and is 1.8 kA for this diode geometry. When the applied axial field was set at 10 kG, the transmitted current was 1.3 kA. The resultant beam conditions are estimated, therefore, to be within the following range:

$$0.033 \leq \beta_\perp(r_w) \leq 0.072$$

and (4)

$$3 \times 10^{-4} \leq \Delta\beta_z/\beta_z \leq 1.4 \times 10^{-3}.$$

For comparison, the computed value for $\Delta\beta_z/\beta_z$ was 9.5×10^{-4} at 10 kG. Even at the upper limit, the beam axial velocity spread is well below that required for collective effects to dominate the interaction. To place this achievement in proper perspective, it should be noted that these velocity spreads are more than an order of magnitude less than those typically associated with electron beams of this intensity.

III. Theory

The analysis of the beam wave interaction in a millimeter-wave free-electron laser is a complex endeavor requiring not only a linear theory to illuminate the interaction physics and to predict gain but also a nonlinear analysis to examine saturation effects and efficiency. To make the linear analysis more tractable, several simplifying assumptions are usually imposed on the model. In the linear theory which follows, a cold electron beam and an ideal helical wiggler field are assumed. Because of the complexity of the saturation phenomena, the nonlinear analysis was performed using a fully electromagnetic numerical simulationof the interaction. Although the code did provide the desired nonlinearcapability, the provision for only one spatial dimension limited the analysis to the idealized wiggler fields. To assess the consequences of this limitation in the linear and nonlinear analysis, the effects of the realistic wiggler fields were investigated with a multi-particle trajectory code. Using this code, the impact of the wiggler field gradients on the velocity spreads of an initially cold beam were studied as a function of the pump strength and the proximity of the guide field to gyroresonance.

A. Linear Analysis

Recent theoretical work[16,17,18] has shed light on the collective interaction in the presence of an axial guide field by perturbation methods about equilibrium orbits. For combined axial guide and helical wiggler magnetic fields, two classes of stable helical equilibrium orbits exist[19,20] with constant velocity v_z and transverse velocity

$$v_\perp = \Omega_w v_z/(\Omega_o - \gamma k_w v_z) \qquad (5)$$

where $\Omega_{o,w} \equiv eB_{o,r}/mc$, $k_w = 2\pi/\lambda_w$, and B_o and B_r are the axial and transverse magnetic fields (see Fig. 6). Group-I orbits occur at low values of the guide field ($\Omega_o < \gamma k_w v_z$) and exhibit high v_z which decreases monotonically with increasing B_o. Such orbits become unstable at a critical value of axial field given by $\Omega_o = \gamma(1 + v_\perp/v_z)^2)^{-1} k_w v_z$. Group-II trajectories exist for all B_o but exhibit high axial velocities only when $\Omega_o > \gamma k_w c$. The growth rate in the limit of stimulated Raman scattering is given by

$$(\mathrm{Im}\ k)_{max} \approx 1/2\ |\beta_\perp|\ (\omega_p k_w \gamma_z \Phi^{1/2}/v_z)^{1/2} \qquad (6)$$

where ω_p is the invariant plasma frequency, and

$$\Phi \equiv 1 - \Omega_o \gamma_z^2\ v_\perp^2/[(v_z^2 + v_\perp^2)\Omega_o - \gamma k_w v_z^3] \qquad (7)$$

Note that the presence of the axial guide field leads to gain enhancement both by increasing the transverse velocity and through Φ which comes from the ponderomotive potential. In the limit of zero beam temperature, the Raman regime is valid as long as

$$\omega_p\ \Phi^{1/2} \gg \frac{1}{8}\ \beta_\perp^2\ \gamma_z^3\ \frac{v_z^2}{c}\ k_w. \qquad (8)$$

Therefore, the Raman regime, in this limit, is accessible even for lower beam densities when an axial field is present and Φ is large. The strong pump regime occurs in the opposite limit and is characterized by a maximum growth rate of the form

$$(\mathrm{Im}\ k)_{max} \approx \frac{3}{2}\ (\frac{\beta_\perp^2}{2}\ \xi^2\ \frac{c}{v_z}\ \Phi)^{1/3}\ k_w \qquad (9)$$

where $\xi \equiv \omega_p/ck_w$ is the beam strength parameter.

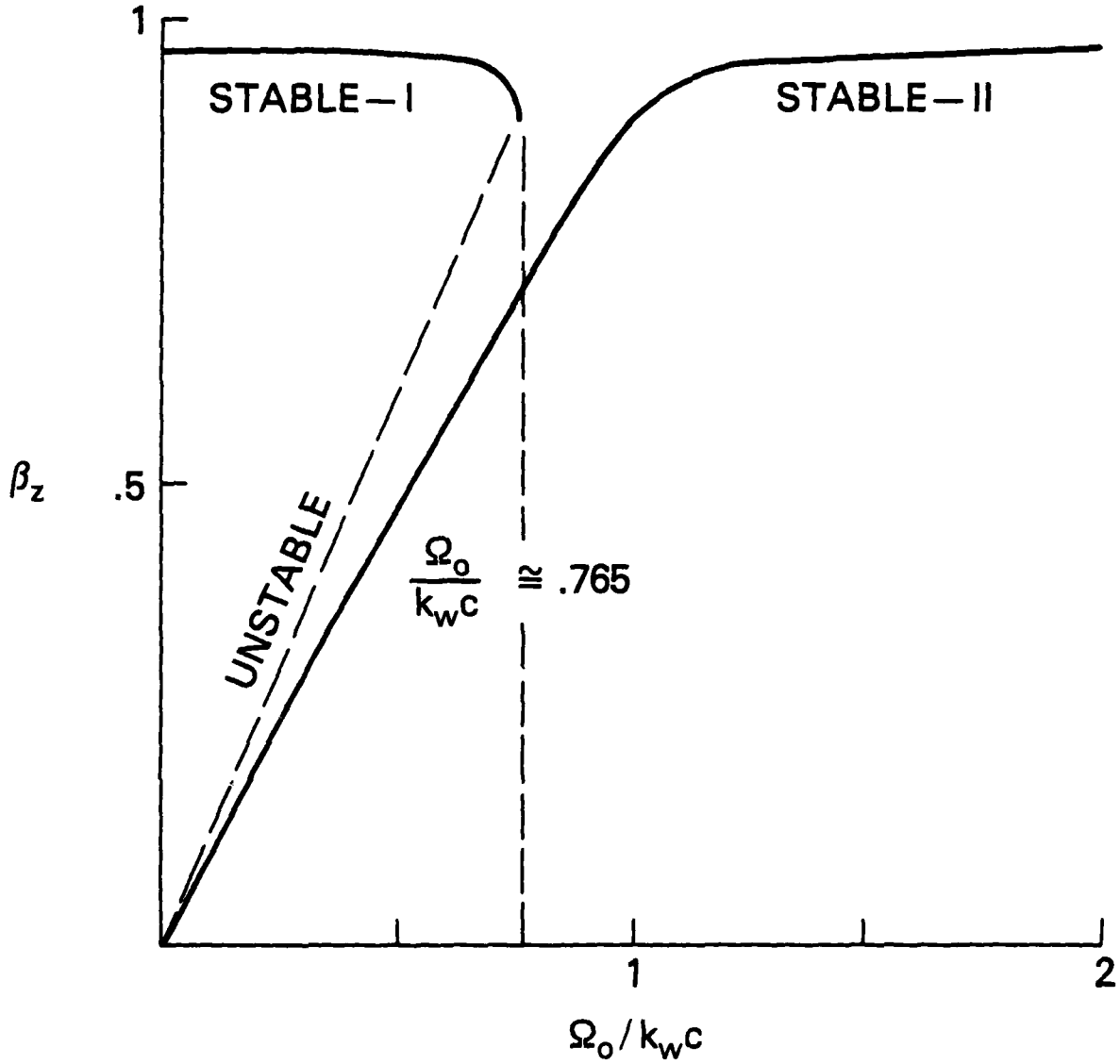

Fig. 6 The two types of stable orbits possible in an ideal wiggler field. The axial velocities are shown as a function of normalized guide field. Note that the type I orbits become unstable at $\Omega_o/ck_w \approx .765$.

A calculation of the maximum gain as a function of B_0 for parameters corresponding to the experiment ($\gamma \sim 3.5$, $B_r \sim 0.63$ kG), using the results of the complete stability theory, is shown in Fig. 7. The dashed line in the figure represents the frequency corresponding to peak gain, and the calculation has been performed only for frequencies greater than the 60-GHz cutoff imposed experimentally. As anticipated, the growth rate increases as the gyroresonance ($\Omega_0 \sim \gamma k_w v_z$) is approached from above or below. The apparent discontinuity shown in the growth rate for group-I orbits at $B_0 \sim 9$ kG corresponds to a transition from a Raman to a strong pump interaction[1]. For guide fields below this value, as well as for group-II trajectories, the gain is given predominantly by the Raman-scattering result. It is important to recognize, however, that nonlinear (saturation), finite geometry, and non-ideal effects are not included in these calculations. As a result, Fig. 7 cannot be used to predict the detailed variation in the output power with B_0, and can only be used to obtain the parametric limits of radiation production and to estimate the small-signal gain.

B. Nonlinear Simulation

The effects of beam temperature on the saturated efficiency of the experiment were studied with a fully electromagnetic, relativistic particle code[21] which included one spatial and three velocity components. Although the electron beam was assumed to be monoenergetic, the electrons were allowed to have random velocities in the directions perpendicular to the beam propagation. Such a scattered electron beam can be modeled according to the momentum distribution function

$$f(p) = \delta(p - p_0)\exp(-p_\perp^2/\Delta p_\perp^2)/[p_0 \Delta p_\perp F(p_0/\Delta p_\perp)] \qquad (10)$$

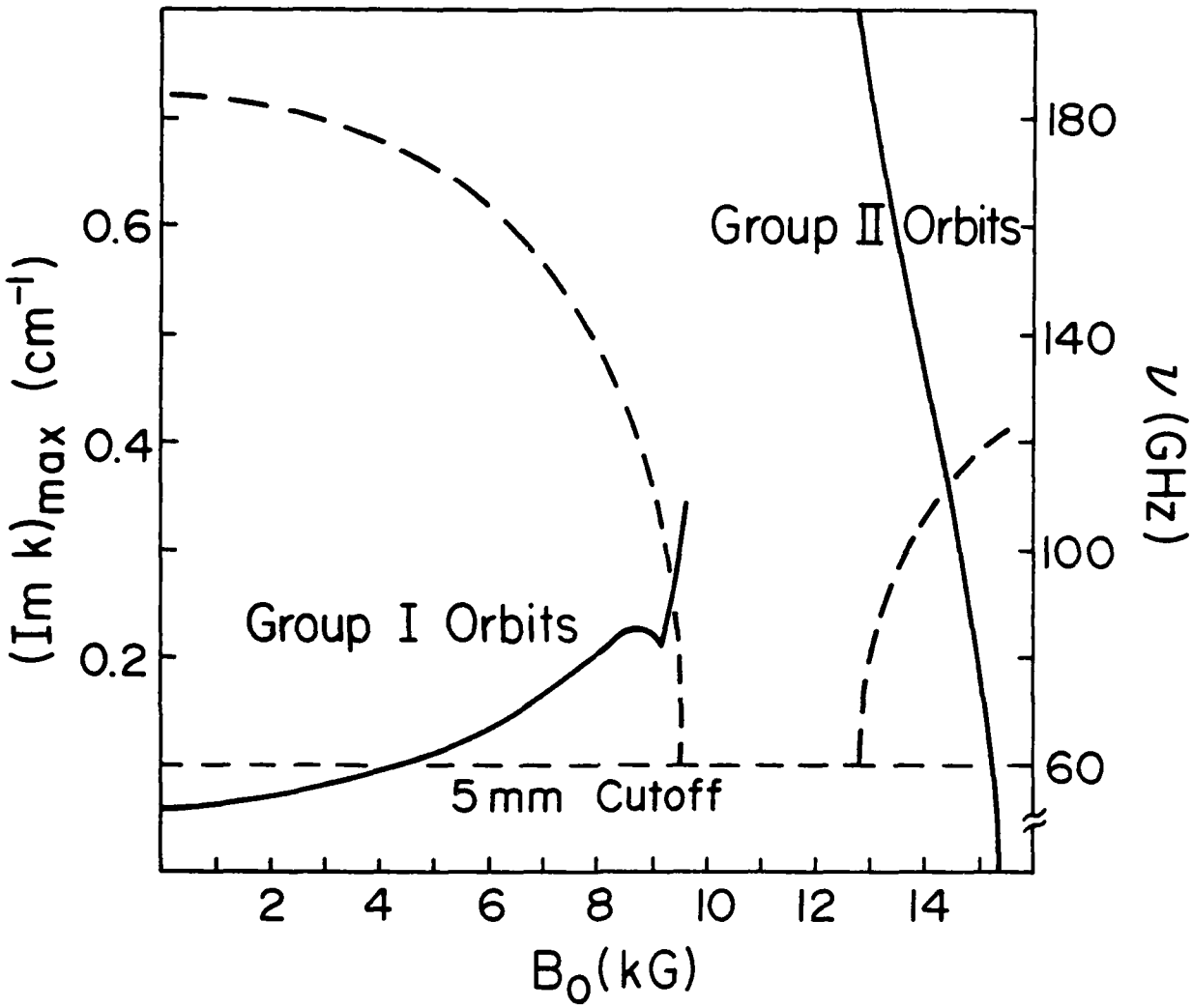

Fig. 7. Calculation of gain (solid lines) and emission frequency (dashed lines) as a function of axial magnetic field for B_r = 0.63 kG. The experimental 5-mm cutoff is shown as a horizontal dashed line. Note that below gyroresonance the gain curve is much flatter than above the resonance.

where $F(x) = \exp(-x^2) \int_0^x \exp(t^2)dt$, p is the particle momentum, $p_o = mc(\gamma^2 - 1)^{1/2}$, and $\Delta p_\perp$ is the FWHM of the perpendicular momentum distribution. For this distribution the spread in axial velocity is given by

$$\frac{\Delta\beta_z}{\beta_z} \simeq \frac{1}{2} \left(\frac{\Delta p_\perp}{p_o}\right)^2 \text{ for } \frac{\Delta p_\perp}{p_o} \ll 1. \qquad (11)$$

The velocity spread produced by (10) represents a true, random temperature, unlike the experimental value which represents the radial dependence of the velocity distribution. The exact correspondence between these types of velocity spread is unclear; however, they are expected to have similar effects on the beam-wave interaction.

Electron beams with a momentum distribution given by (10) were initialized self-consistently in the simulations. The simulations had an immobile ion background to provide the necessary electrostatic neutralization and periodic boundary conditions for the electromagnetic fields and the beam particles. The simulation parameters were chosen to match experimental values to the degree possible.

The dependence of the efficiency of energy transfer from the electron beam to the RF wave is illustrated in Fig. 8. The striking result is that the efficiency drops dramatically when the momentum spread increases slightly from 0 to .65%. However, after the initial sharp drop, it becomes rather insensitive to the spread. It should be noted that the efficiency, as shown in Fig. 8, takes into account the energy of all unstable electromagnetic modes. This rather surprising result from the simulations shows a completely different nonlinear behavior for the free-electron laser interaction than might be expected from the effects of momentum spread on the saturation by electron trapping of the relativistic two-stream instability[22].

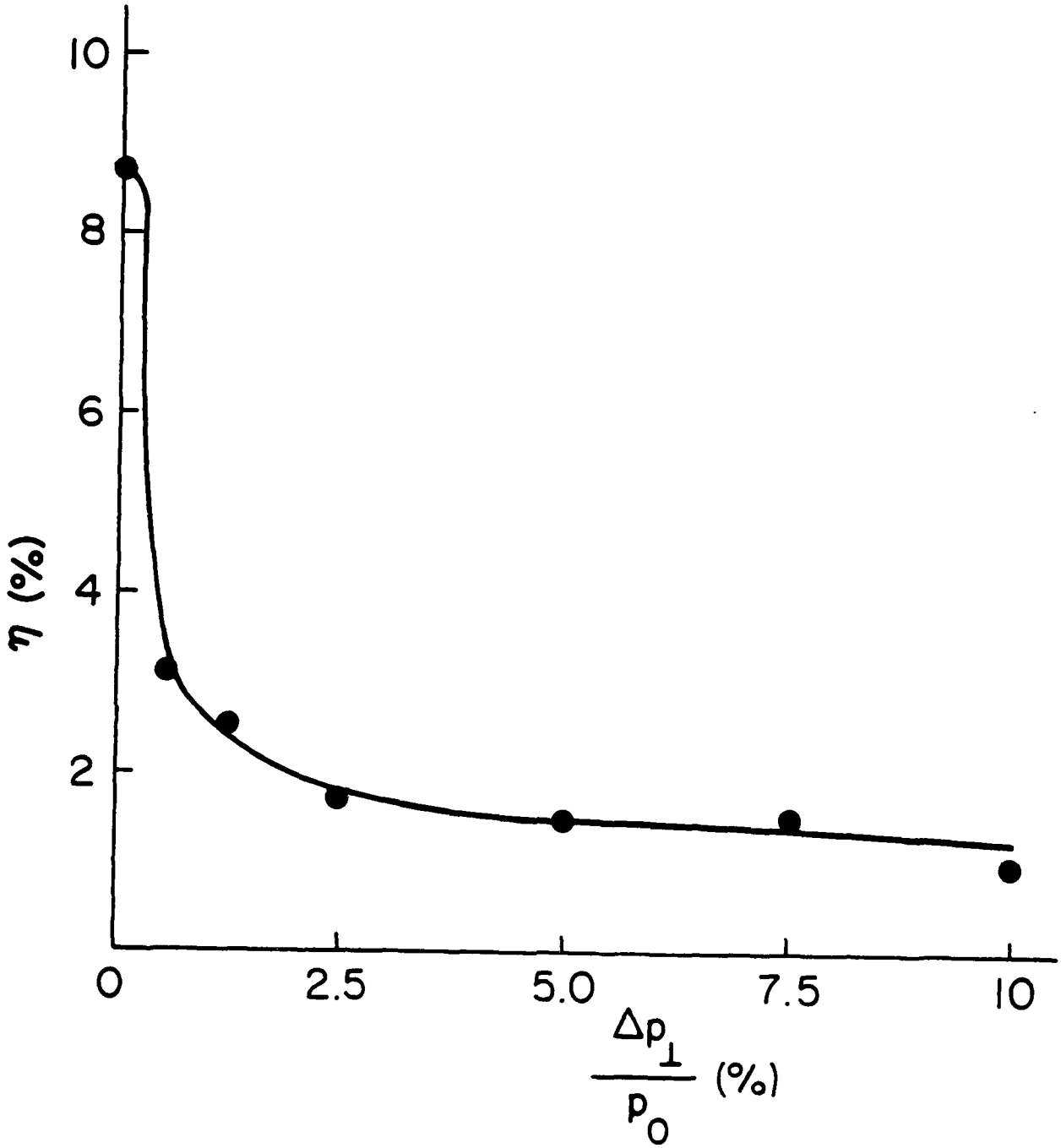

Fig. 8 Electron-beam-power to RF-power conversion efficiency as a function of momentum spread. The 0.1% velocity spread observed in the experiment corresponds to a momentum spread of 4.5% (see Eq. 11).

The simulations are considered to be accurate representations of the experiment provided that three dimensional effects are not dominant,and that the code electron beam adequately models the experimental beam. For a beam with the velocity spread observed in the experiment (≈ .1%), simulations predict an efficiency of roughly 2%. This value is remarkably close to the 2.5% peak efficiency observed in the experiment. Because of the previously mentioned differences between the simulations and the experiment, some caution should be exercised in applying the code results to interpret the experiment. Nonetheless, the good agreement between the experiment and the simulations is noteworthy, and supports the beam quality calculations and measurements discussed earlier.

As shown in the Experimental Results section there are definite combinations of the wiggler and guide magnetic fields which determine the onset, maximum, and cutoff of radiation production. The spatial evolution of the electromagnetic radiation for three sets of experimental parameters which correspond to these conditions is shown in Fig. 9. At radiation onset, the simulation shows that the linear growth rate of the instability was so small that the electromagnetic energy could not achieve an appreciable amplitude within the length of the wiggler. Thus, a change of magnitude of the wiggler field and/or the guide field to enhance the transverse velocity of the electron beam would increase the output of radiation. This is illustrated in the second case in Fig. 9. The electromagnetic energy saturated at a high level at about two-thirds of the wiggler length. The fact that the electromagnetic energy did not decay away as the electron beam continued to interact with the wiggler field indicates that the coherence of the electron bunching was not destroyed. Consequently, the electron beam could still deposit energy into other unstable electromagnetic modes. The third case shown in Fig. 9 had the highest wiggler field, and showed a strong linear growth of the instability. However, the instability saturates in a relatively short

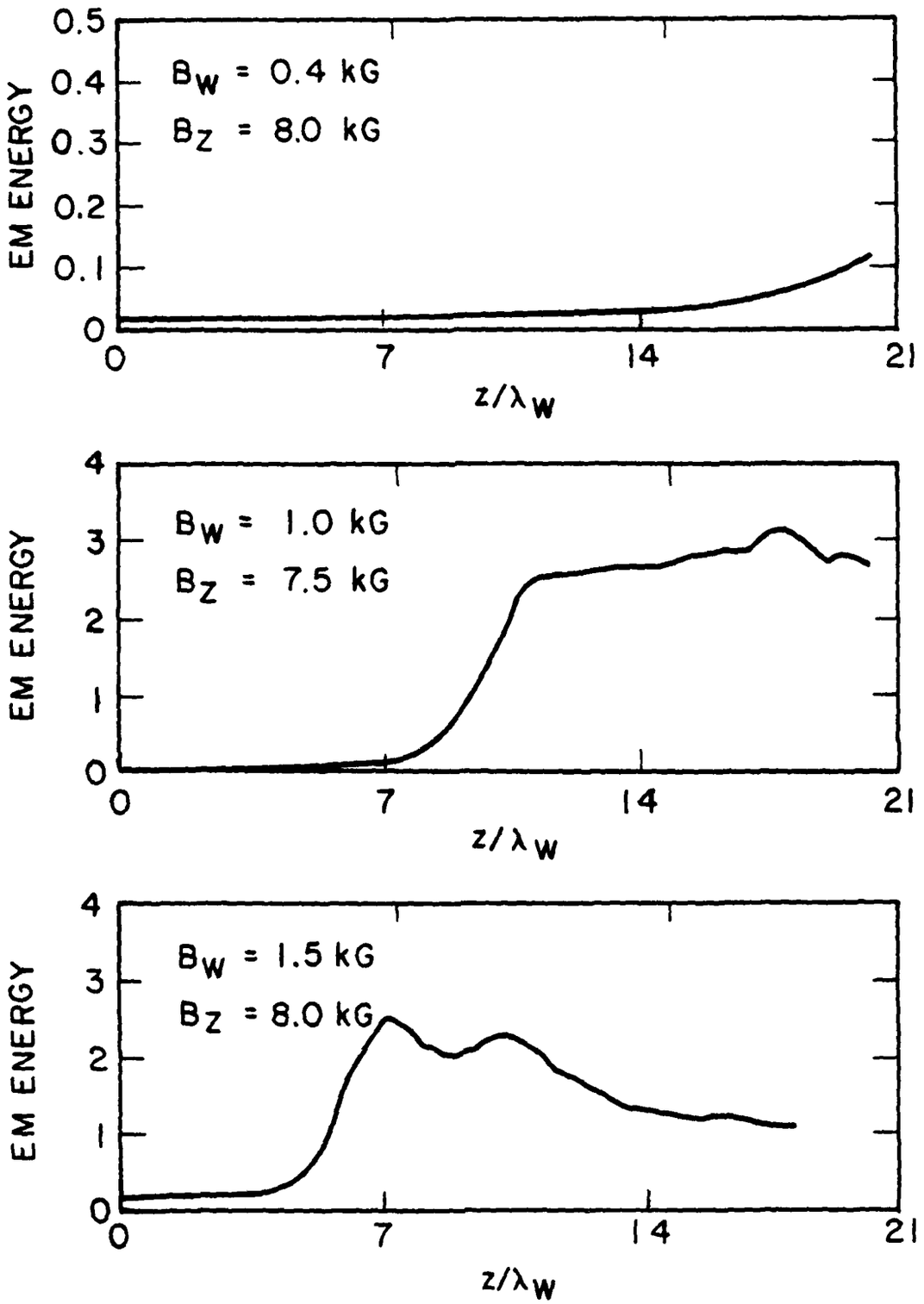

Fig. 9 Spatial growth of electromagnetic energy for field values corresponding to the onset, maximum, and cutoff of power in the experiment. The axial distance is normalized by the wiggler period (λ_W = 3 cm), and the simulations start in the uniform wiggler section.

distance and the total electromagnetic energy decays due to strong wave-particle interaction. As a result, the emitted power is significantly reduced.

C. Realistic Wiggler Effects

Neither the linear analysis nor the nonlinear simulations took into account the beam transition into the wiggler and the spatial variation of the actual wiggler field. To evaluate these effects, a multiple-particle trajectory integration code was developed and used to study beam propagation in the first-order wiggler fields and in a finite geometry waveguide[23]. A comparison of calculated and measured current transmitted through the wiggler is shown in Fig. 10 for an effective wiggler field of 0.7 kG. Since the initial current in the code is normalized to 1kA and diode phenomena which affect the injected current (see Fig. 5) are not included, a superficial disagreement exists for fields less than 6 kG. With that exception, the agreement is excellent, and the features predicted by the idealized-wiggler orbit theory are clearly present. The rapid decrease in current at 9.5 kG results from current loss to the waveguide wall as the group-I orbits become unstable at the critical value of axial magnetic field. Increased propagation in group-II orbits is seen above 11.5 kG as the wall losses progressively decrease.

The wiggler used in the experiment was designed to provide an adiabatic entrance for the beam (see Fig. 2). Calculations incorporating the experimental wiggler profile indicate that the transition is adequate, but not perfect. As a result the electrons in the uniform section of the helix oscillate about the ideal equilibrium orbits. At modest pump levels and for fields far from resonance, the oscillations are small; however, as gyroresonance is approached or as the pump level is increased, the amplitudes of the oscillations increase dramatically. This velocity oscillation can act as an effective temperature because of the slippage between the beam and the RF wave as the wiggler is traversed.

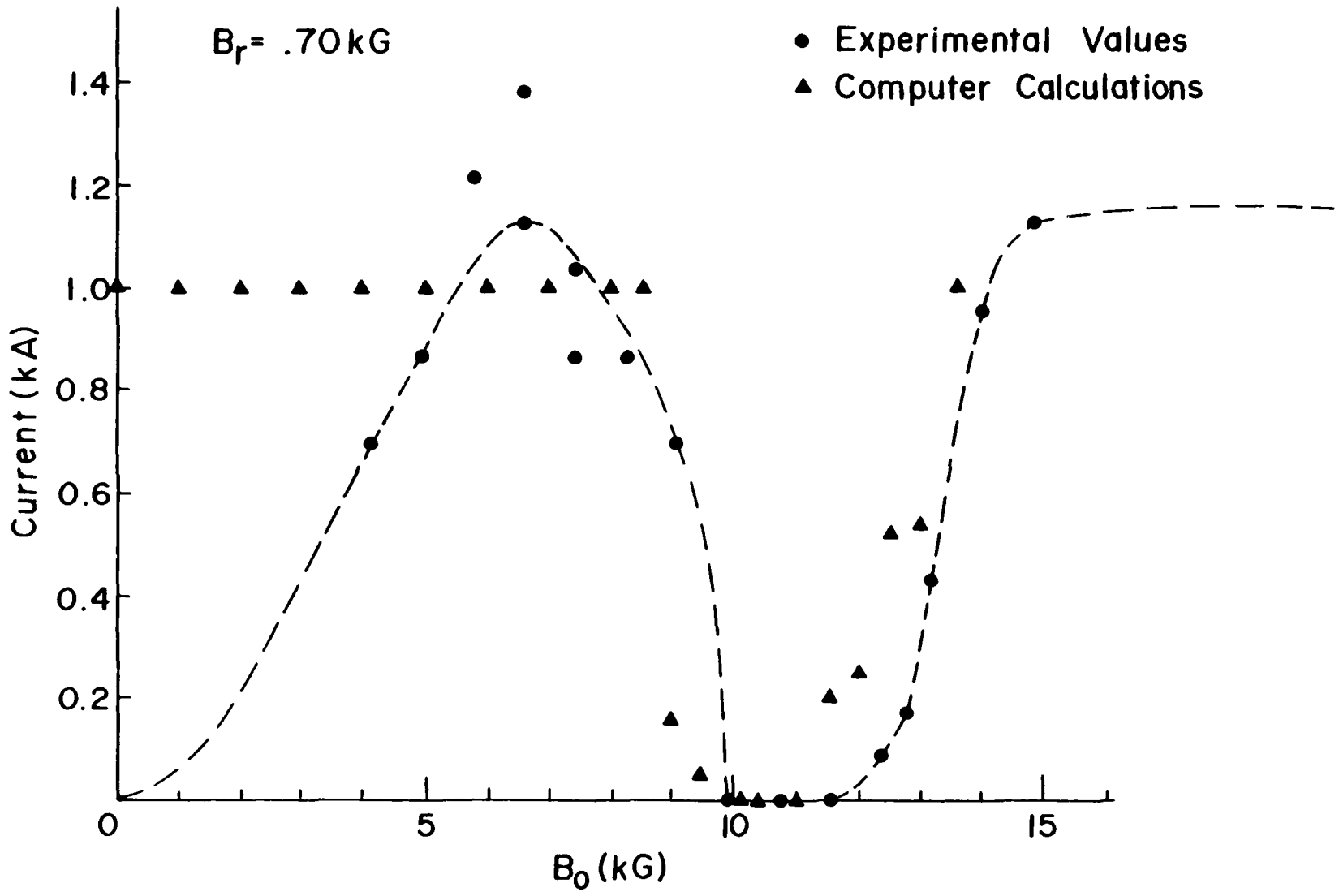

Fig. 10 Transmitted current at the wiggler exit as a function of axial guide field.

The spatial variation of the first order wiggler field induces a cross-sectional velocity spread. The magnitude of this spread depends upon the beam area, wiggler period, pump amplitude, proximity to gyroresonance, and whether the axial field is above or below the "transition" field of the wiggler. The transition field is given by

$$B_T = \frac{mc^2}{e} \gamma k_w (\beta_z^2 + \beta_\perp^2)^{1/2} \tag{12}$$

and represents the axial field above which the denominator of (5) can not be driven to zero for any value of pump field. The dependence of the velocity oscillation and the velocity spread on pump strength is shown in Fig. 11 for guide fields above (15 kG) and below (10 kG) the transition field. Note the striking difference in the behavior between the two cases as the pump level approaches a critical value at which the orbits become unstable. The open circles on the graph indicate field values at which the beams have the same average velocity. In general, the code results show that for beams with the same average velocities, operation below the transition field or closer to gyroresonance leads to larger velocity spreads.

The effects of operating near gyroresonance are shown in Fig. 12. Since the resonant denominator in (5) acts to enhance the effects of field differences, the beam becomes more sensitive to field variations near the gyroresonance. This rapid beam thermalization near gyroresonance will act at some point to offset the effects of increased $v_\perp$ in producing an enhanced gain. The cold-beam limits shown in Figs. 11 and 12 indicate the ranges of field strengths where this is likely to occur. Experimentally, peak RF emission occurs in the regions before the cold-beam limit is reached (cf. Fig. 13). The effect of these velocity spreads on the interaction is not clear, because the spreads are not random. However, at some level, these macroscopic spreads are expected to degrade the interaction in a manner similar to a true temperature.

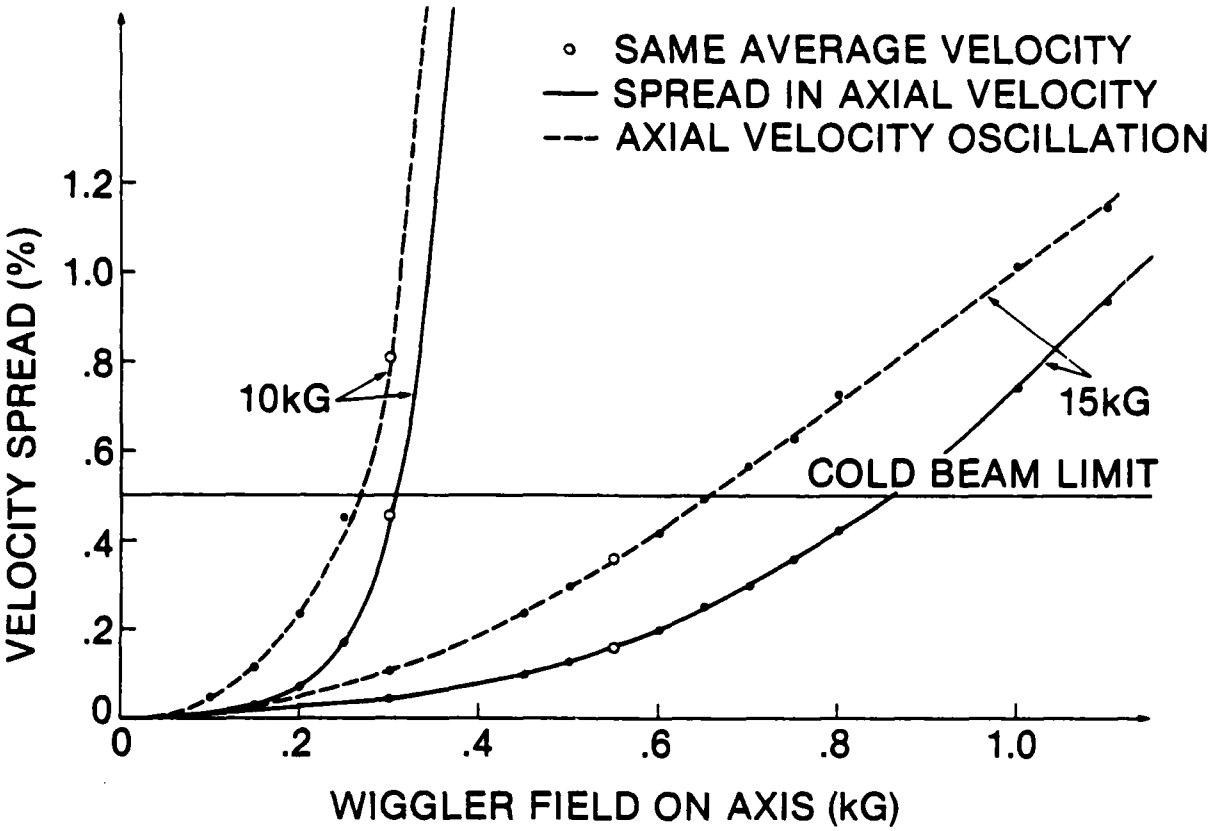

Fig. 11 The two types of velocity spread induced by the actual wiggler field. The solid curves show the cross sectional velocity spread due to the field gradients and the dashed curves are the velocity oscillations induced by the adiabatic entrance. The 10-kG curves are below, and the 15-kG curves are above the 12-kG transition field of the experiment. The cold beam limit is derived from the theoretical expression $(\gamma - 1)\omega p/2\gamma\gamma_z^3 c\, k_w \gg \delta\beta_z$.

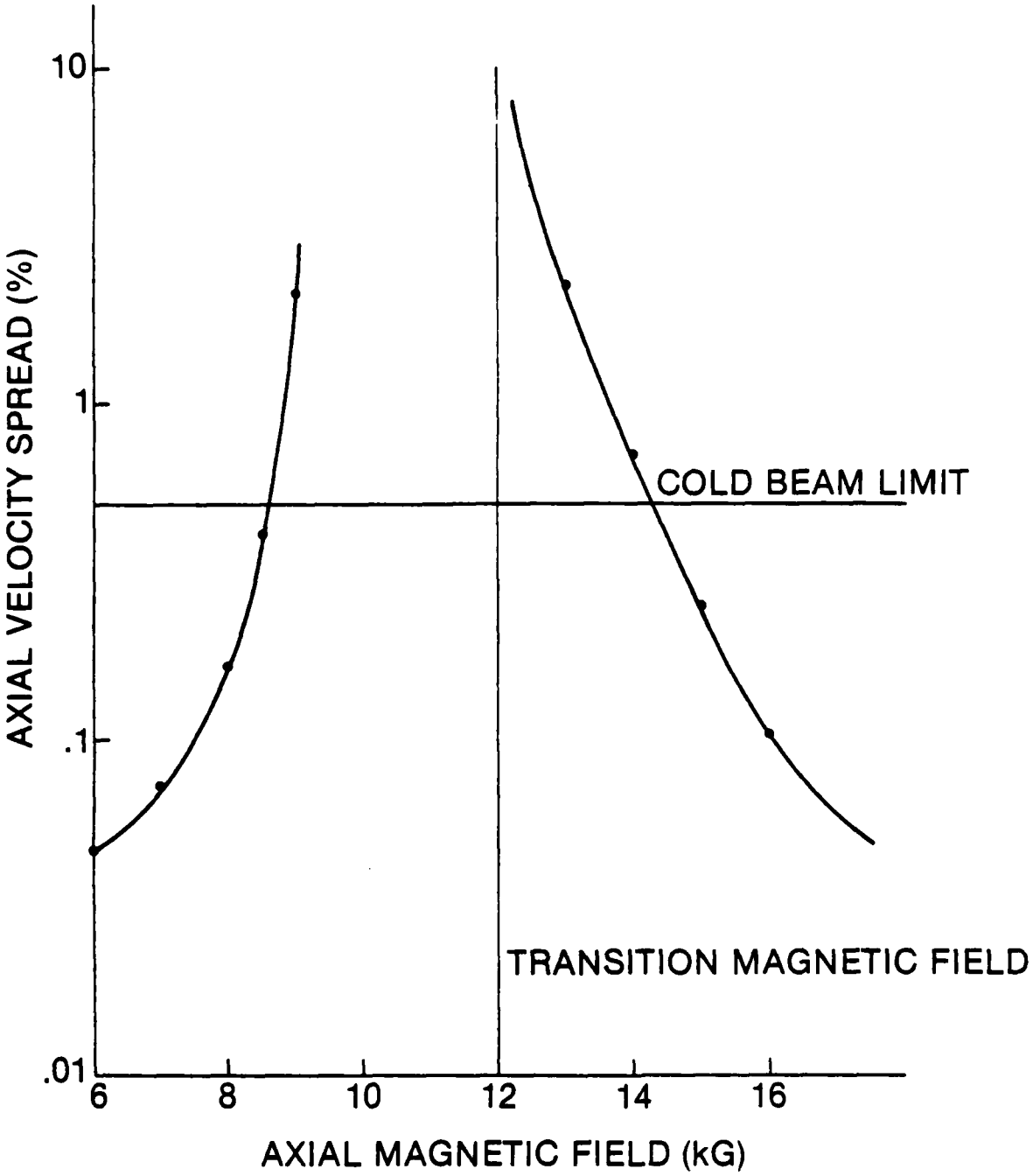

Fig. 12 Axial velocity spread induced by first order wiggler field gradients near gyroresonance. The wiggler field amplitude is the same as in Fig. 10, Br = .70 kG.

IV. Experimental Results

A plot of radiated power as a function of axial field strength is shown in Fig. 13 for the interaction parameters used in Fig. 7. This radiated power profile represents a complex overlay of interactive phenomena of which three are thought to dominate. The primary issues are the quality of the injected beam (Figs. 5 and 10); the three dimensional effects of the wiggler fields on the electron trajectories (this effect is most pronounced near gyroresonance, Figs. 10 and 12); and the variation of the gain with the experimental parameters (Fig. 5). The onset of measurable power at low guide field is related to the increase in transmitted current with increasing B_0. The subsequent drop in power at 10 kG is consistent with the transition to unstable orbits and the rapid thermalization of the beam. Above gyroresonance ($B_0 \approx 11.5$ kG), the wavelength of the radiation produced by group-II orbits will decrease as the axial velocity is increased. The 5-mm cutoff imposed by the filter corresponds to the theoretically predicted value of $B_0 = 12.5$ kG which is in close agreement with the experimental value. The comparatively slow rise in radiated power from 12.5 kG to 15.0 kG is consistent with the progressive improvement in beam quality shown in Fig. 12. The decrease in power at higher values of B_0 corresponds to a loss of gain as shown in Fig. 7. Note that the power production below gyroresonance is not as peaked in guide field as above gyroresonance. This result is in agreement with the flatter gain curve in Fig. 7 and the more rapid beam thermalization shown in Fig. 12.

Data have been compiled over a range in pump field extending from 0.2 to 2.4 kG. The salient features of the observed parametric variation can be summarized by identifying the pump strength at which thresholds for measurable power and the point of maximum power occur as a function of the guide field. The resultant plot is shown in Fig. 14.

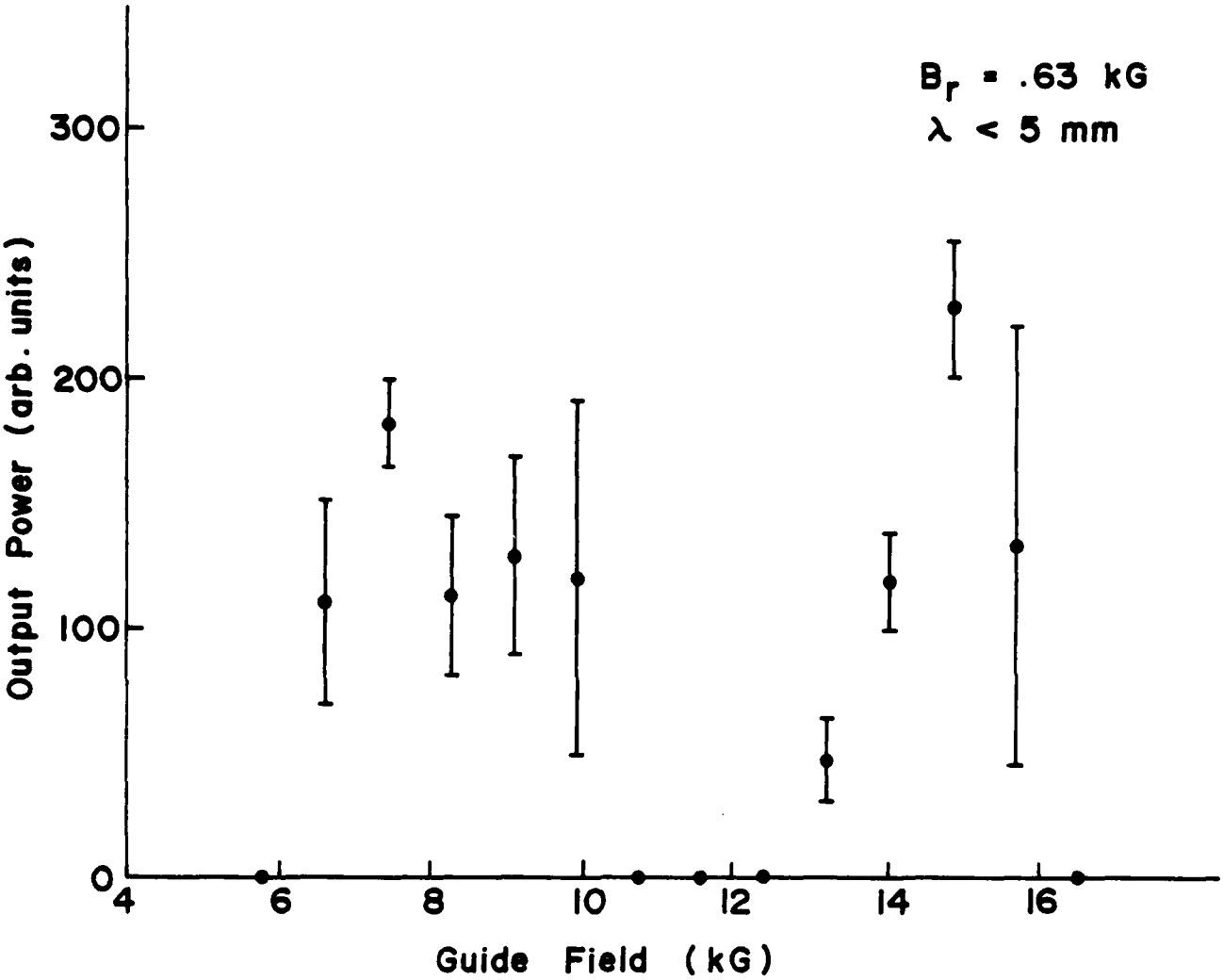

Fig. 13. Measured variation in output power ($\lambda < 5$ mm) with guide field for $B_r = 0.63$ kG. The error bars represent the shot-to-shot reproducibility of the experimental parameters and are based on five or more shots.

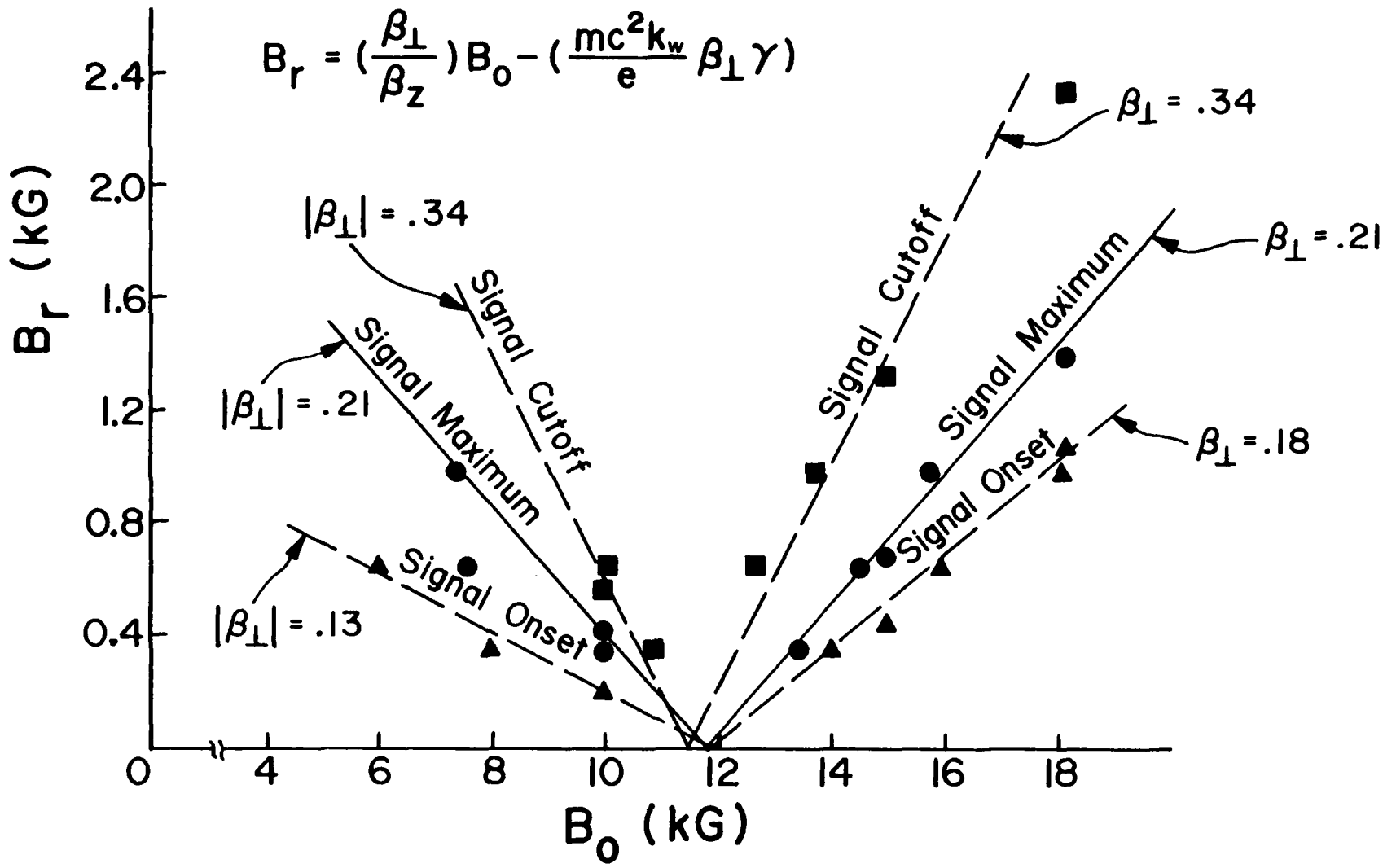

Fig. 14. Signal variation with pump and guide magnetic fields. Signal onset, maximum, and cutoff are plotted as triangles, circles, and squares respectively. The lines correspond to constant values of $\beta_\perp$.

Rewriting (5) yields the following relation between the transverse and longitudinal electron velocities and the pump and guide fields:

$$B_r = (\beta_\perp/\beta_z)B_o - (mc^2k_w/e)\beta_\perp\gamma. \qquad (13)$$

From this equation, it is evident that the conditions for constant transverse and axial velocities are defined by pairs of straight lines which intersect the horizontal axis at the resonant guide field. The free-electron laser interaction is much more strongly dependent on these velocities than on particular values of magnetic field. Specific experimental features should lie on straight lines characterized by unique values of transverse velocity. Note that the lines in Fig. 14 are not best fits to the data, but are calculated using (13) assuming particular values of transverse velocity. The observed agreement between experimental results and calculations based on ideal single-particle trajectories is another indication that the electron beam is very cold.

The magnitude of the radiated power in the free-electron laser interaction is related through the gain to the transverse velocity and has only a weak dependence on the magnetic fields which occurs though $\Phi^{1/4}$ (see Eq. (6)). The cyclotron maser instability, on the other hand, is sensitive to particular values of the guide field as well as the transverse velocity. Previous intense beam cyclotron maser experiments[24-28] have typically shown a power increase of two-to-three orders of magnitude at specific axial guide fields. In light of this, it is worth noting that the peak power observed along the $\beta_\perp = .21$ lines in Fig. 14 is constant to within a factor of two for all the guide fields tested. The differences in peak power appear to be related to beam quality issues. The highest powers are observed above 15 kG where the injected beam quality is highest and the thermalization effects of the gyroresonance are minimized.

The measure of the constancy of β_z along the lines defined by (13) is the radiated wavelength. To examine this scaling, the wavelength of power generated at 15 and 18 kG was measured at the power threshold conditions of $\beta_\perp = 0.18$ and $\beta_\perp = 0.34$. The frequency was determined by observing the threshold for transmission through a sequence of high-pass filters. On the high-$\beta_\perp$ threshold, the break in transmitted power occurred between cutoff frequencies of 63 and 68 GHz at both values of B_0. The corresponding bounds for the low-$\beta_\perp$ threshold were between 103 and 117 GHz. An analysis of the uncoupled dispersion curves for the pump-shifted, negative-energy, space-charge wave and the TE_{11} waveguide mode indicates that the intersections of interest occur at 60 and 117 GHz, respectively. Wavelength measurements at the peak power points using both cutoff filters and a grating spectrometer indicate a frequency of 80 GHz which is also in agreement with the dispersion analysis. Independent measurements have established that the observed radiation pattern is consistent with that of the TE_{11} mode.

Calculations of spontaneous emission suggest that the uncorrelated noise spectrum corresponds to a few tens of milliwatts of radiated power. Direct measurement of the emission in the absence of a pump field shows less than 10 W of total power in the range of a W-band detector (60-110 GHz). Calorimetry measurements of the peak observed emission detect 0.68 J, corresponding to ~ 35 MW in a 20-nsec output pulse and an instantaneous efficiency of 2.5%. This suggests at least fifteen power e-foldings, corresponding to a gain length of approximately 4 cm. Theory (Fig. 7) suggests a gain length of several centimeters, in good agreement with this value.

V. Summary

Initial measurements on a new high-power, short-pulse, millimeter-wave free-electron laser experiment have been completed. These measurements have demonstrated high-power superradiant emission, corresponding to an instantaneous conversion efficiency of electron beam energy into millimeter-wave radiation of 2.5%. This efficiency is an order of magnitude improvement over that seen in other millimeter-wave free-electron laser devices. Computer simulations and experimental measurements have shown that the quality of the electron beam extracted from the apertured diode is well in excess of that required to sustain a collective beam-wave interaction. The experiment has shown a regular parametric dependence on guide and pump fields both above and below gyroresonance; a dependence that had not been previously reported. Measurements of radiation onsets and cutoffs agree with predictions based on single-particle orbits and a new cold-beam Raman theory. The observed scaling of wavelength, emitted power, and gain are in excellent agreement with the assumption of a Raman free-electron laser interaction. Computer simulations of the nonlinear effects in the experiment show good agreement with the power scaling and efficiency observed in the experiment. The simulation results taken together with the realistic wiggler analysis indicate that thermal effects are limiting the experimental efficiency. It is not yet known whether this limit is imposed by the injected beam quality, the wiggler gradients, or by some other mechanism.

Acknowledgments

The authors would like to thank L. Friedland, P. Sprangle, A. Drobot, L. Thode, and C. Snell for useful discussions. This research was supported by the Naval Air Systems Command under Contract No. WF32-389-592, and by the Air Force Office of Scientific Research under contract to North Carolina State University.

References

1. P. Sprangle, R. A. Smith, and V. L. Granatstein, "Free Electron Lasers and Stimulated Scattering from Relativistic Electron Beams," in Infrared and Millimeter Waves, ed. K. J. Button (Academic, New York, 1979), Vol. I, p. 279.

2. V. L. Granatstein and P. Sprangle, "Mechanisms for Coherent Scattering of Electromagnetic Waves from Relativistic Electron Beams," IEEE Trans. Microwave Theory Tech. MTT-25, pp. 545 (1977).

3. D. B. McDermott, T. C. Marshall, S. P. Schlesinger, R. K. Parker, and V. L. Granatstein, "High-Power Free-Electron Laser Band on Stimulated Raman Backscattering," Phys. Rev. Lett. 41, 1368 (1978).

4. T. C. Marshall, S. Talmadge, and P. Efthimion, "High-Power Millimeter Radiation from an Intense Relativistic Electron-Beam Device," Appl. Phys. Lett. 31, 320 (1977).

5. A. N. Didenko, A. R. Borisov, G. P. Fomenko, E. G. Furman, A. V. Kozhevnikov, A. M-S Le, G. V. Melnikov, Yu. G. Stein, and R. G. Zerlitsin, "Experimental Investigation of Stimulated Microwave Radiation from Intense Relativistic Electron Beams," in Abstracts of the International Topical Conference on High Power Electron and Ion Beam Research and Technology, Palaiseau, France, 1981 (unpublished).

6. R. H. Jackson and R. K. Parker, "Sources of Beam Temperature in the Electron Gun of a Raman FEL," Abstracts of the 1980 IEEE International Conference on Plasma Science.

7. R. K. Parker, R. H. Jackson, S. H. Gold, H. P. Freund, V. L. Granatstein, P. C. Efthimion, M. Herndon, and A. K. Kinkead, "Axial Magnetic-Fiel Effects in a Collective-Interaction Free-Electron Laser at Millimeter Wavelengths," Phys. Rev. Lett. 48, 238 (1982).

8. J. R. Bettis, J. K. Burton, R. K. Parker, S. H. Gold, M. Herndon, R. H. Jackson, A. K. Kinkead, A. H. Guenther, and E. J. Kobiela, "Laser-Triggered Switch Modification to VEBA," IEEE Trans. Nucl. Sci. NS-28, 3091 (1981).

9. S. H. Gold, R. H. Jackson, R. K. Parker, V. L. Granatstein, P. C. Efthimion and M. Herndon, Raman Free Electron Laser Experiment," Bull. Am. Phys. Soc. 25, 947 (1980).

10. H. Poritsky, "Helical Fields," J. Appl. Phys. 30, 1828 (1959).

11. R. H. Jackson, Ph.D. Thesis, North Carolina State University, in preparation.

12. W. B. Herrmannsfeldt, "Electron Trajectory Program (SLAC Program)," SLAC-166 Report, September 1973 (unpublished).

13. On the VEBA accelerator, as on other pulse charged machines, prepulse is a capacitively-coupled voltage which appears on the diode during the charging of the pulse-forming line.

14. Perveance is defined by $k = I(\text{amps})/V^{3/2}$ (volts) and is invariant for non-relativistic voltages and space-charge-limited emission, i.e., it depends only on the diode geometry.

15. R. K. Parker, R. E. Anderson, and C. V. Duncan, "Plasma - Induced Field Emission and the Characteristics of High-Current Relativistic Electron Flow," J. Appl. Phys. 45, 2463 (1974).

16. H. P. Freund, P. Sprangle, D. Dillenberg, E. H. da Jornada, R. S. Schneider and B. Liberman, "Collective Effects on the Operation of Free Electron Lasers with an Axial Guide Field," Phys. Rev. A, accepted for publication.

17. H. P. Freund, P. Sprangle, D. Dillenburg, E. H. da Jornada, B. Liberman, and R. S. Schneider, "Coherent and Incoherent Radiation from Free-Electron Lasers with an Axial Guide Field," Phys. Rev. A24, 1[illegible]5 (1981).

18. W. A. McMullin and R. C. Davidson, "Low Gain Free Electron Laser Near Cyclotron Resonance," (to be published).

19. L. Friedland, "Electron Beam Dynamics in Combined Guide and Pump Magnetic Fields for Free Electron Laser Applications," Phys. Fluids 23, 2376 (1980).

20. H. P. Freund and A. T. Drobot, "Relativistic Electron Trajectories in Free Electron Lasers with an Axial Guide Field," Phys. Fluids 25, 736 (1982).

21. T. Kwan and C. M. Snell, "On the Efficiency of Free-Electron Lasers with a Scattered Electron Beam," submitted to Physics of Fluids.

22. L. E. Thode, "Plasma Heating by Scattered Relativistic Electron Beams: Correlations Among Experiment, Simulation and Theory," Phys. Fluids, 19, 831 (1976).

23. R. H. Jackson, R. K. Parker, S. H. Gold, V. L. Granatstein, H. P. Freund, P. C. Efthimion, M. Herndon, and A. K. Kinkead, "Axial Field Effects in a Raman Free-Electron Laser," Bull. Am. Phys. Soc. 26, 909 (1981).

24. M. Friedman, D. A. Hammer, W. M. Manheimer, and P. Sprangle, "Enhanced Microwave Emission Due to the Transverse Energy of a Relativistic Electron Beam," Phys. Rev. Lett. 31, 752 (1973).

25. V. L. Granatstein, M. Herndon, R. K. Parker, and P. Sprangle, "Coherent Synchrotron Radiation from an Intense Relativistic Electron Beam," IEEE J. Quantum Electronics QE-10, 651 (1974).

26. S. Talmadge, T. C. Marshall, and S. P. Schlesinger, "Correlation of Intense Electron Beam Dynamics with the Operation of the Relativistic Cyclotron Maser," Phys. Fluids 20, 974 (1977).

27. V. L. Bratman, N. S. Ginzburg, G. S. Nusinovich, M. I. Petelin, and P. S. Strelkov, "Relativistic Gyrotrons and Cyclotron Autoresonance Masers," International Journal of Electronics 51, 541 (1981).

28. R. E. Shefer and G. Bekefi, "Cyclotron Emission from Intense Relativistic Electron Beams in Uniform and Rippled Magnetic Fields," International Journal of Electronics 51, 569 (1981).

END

FILMED

9-83

DTIC